High specific energy asymmetric supercapacitor based on alpha-manganese dioxide/activated expanded graphite composite and activated carbon-polyvinyl alcohol

Phathutshedzo Murovhi, Delvina Japhet Tarimo, Kabir O. Oyedotun and Ncholu Manyala*

Department of Physics, Institute of Applied Materials, SARChI Chair in Carbon Technology and materials, University of Pretoria, Pretoria 0028, South Africa.

*Corresponding author's email: ncholu.manyala@up.ac.za, Tel: (+27) 12 420 3549

HIGHLIGHTS

- α-MnO_2, AEG and α-MnO_2/AEG composite were synthesized through hydrothermal method.
- Introduction of AEG has improved the electrochemical performance of α-MnO_2.
- α-MnO_2/AEG was used as a positive electrode and AC-PVA as negative electrode.
- •The assembled device revealed great supercapacitive characteristics.

ABSTRACT

In this study, alpha-manganese dioxide/activated expanded graphite (α-MnO_2/AEG) composite was successfully synthesized using simple hydrothermal method. Morphology, structure, elemental composition and specific surface area of the material were characterised by scanning electron microscope (SEM), high resolution transmission electron microscope (HRTEM), energy-dispersive spectroscopy (EDS), X-ray diffraction (XRD) spectroscopy, Raman spectroscopy, infrared Fourier transform spectroscopy (FTIR) and Brunauer-Emmett-Teller (BET) method. Electrochemical evaluations were achieved using three- and two-electrode configurations in 1 M Na_2SO_4 electrolyte. The maximum specific capacitance of 185.5 F g^{-1} at 1 A g^{-1} was recorded for three-electrode measurements. The half-cell retained an efficiency of 99.7 % over 2000 cycles at 5 A g^{-1}. The fabricated device using α-MnO_2/AEG composite and activated carbon-polyvinyl

alcohol (AC-PVA) as positive and negative electrodes, respectively, showed a remarkable capacitive property with a specific energy of 33 Wh kg^{-1} and specific power of 999 W kg^{-1} at 1 A g^{-1} within 2.0 V cell potential. Great stability of 97.8 % was observed at a specific current of 5 A g^{-1} for over 10, 000 cycles. Further stability of the device was confirmed by performing a voltage holding of up to 70 h and retained 70 % of its initial capacitance at 5 A g^{-1}.

KEY WORDS: Supercapacitor, hybrid, alpha-manganese dioxide, activated expanded graphite (AEG), activated carbon-polyvinyl alcohol (AC-PVA)

1. INTRODUCTION

The rise in population as well as high consumption of fossils fuels, which cause global warming has resulted in a global crisis in the energy industry due to the ever increasing demand for energy and its related cost [1]. To combat these global issues we require a substitute of energy sources such as, hydropower energy, solar energy, wind energy and geothermal energy [2]. However, these energy sources do not provide sufficient energy due to atmospheric conditions and hence effective energy storage devices are required. Electrochemical devices such as supercapacitors (SCs) which are bridging gap between batteries and conventional capacitor are very efficient in this regard. Efficiency of supercapacitors is attributed to system mechanism which delivers long cyclic stability, rapid charge/discharge capabilities and high specific power [3]. Supercapacitors are categorised into two types, namely electric double layer capacitors (EDLCs) and pseudocapacitors. Mechanism of storing charge by means of charge separation in a small distance on electrode/electrolyte interface is applicable for EDLCs whilst in pseudocapacitors faradic-type

mechanism of charge transfer resulting in a capacitance which is not electrostatic in nature is endorsed [4].

Carbon derivative materials such as carbon nanorods, carbon nanotubes, activated carbon, and carbon nanofibers exhibit high specific surface area and good conductivity which enables them to be used in SC applications. These properties of carbon based materials make it favourable for fabrication as a negative electrode for SC [5][6][7][8][9][10][11]. Activated carbon have been synthesised from different biomass such as coconut shell and wood [12][13][14][15]. Moreover, advancement in technology and synthesis methodologies, have opened up door for fabrication of supercapacitors from other materials including fish scale [16], coffee beans [17] and pine cones [18]. However, their capacitance is very low and so as the specific energy which require improvement for commercial applications.

Some of the transition metal oxides include cobalt, manganese, ruthenium and, nickel oxide [19][20][21][22][23] have attracted many researchers due to their pseudocapacitive behaviours. Amongst those, manganese oxides are of great potential due to fast diffusion performance, redox reversibility, cost-effective and environmentally friendly [24][13]. Manganese oxides based electrodes have charge storage mechanism which is faradic due to shuttle of redox reaction between Mn (IV) and Mn (III) in outer active sites [25]. They have been studied extensively based on their properties such as crystallographic structure, copious oxidation states and wide potential window which can be polarized to higher evolution [26][23]. Manganese dioxide is categorised by three different polymorphs which result from different links of MnO_6 octahedral units such as α-, β-, δ- and ε- types [27]. The α-MnO_2 has a wider 2x2 tunnels (~ 4.6 Å) which provides advantage of high diffusion rate and storage of large size electrolyte cations which contribute to high specific

capacitance [28]. However, experimentally the specific capacitance of MnO_2 is in the range of 150 - 350 F g^{-1}, though, theoretically is 1370 F g^{-1} [29]. This is due to poor electron conductivity which reduces cycling performance and limits further application in energy storage system [28]. Therefore, to overcome such setbacks MnO_2 can be synthesized by incorporation of carbon materials like activated carbon and form a composite with improved properties that combine both advantage and disadvantage of transition metal and carbon-based materials [30][31][32][33][34][35].

Furthermore, researchers have moved away from using organic electrolytes due to their effect in the environment. On the other hand aqueous electrolytes are high in ionic conductivity, non-toxic, fairly safe and non-corrosive [23]. The disadvantage of aqueous electrolytes is the limitation on the potential window (1.23 V) due to decomposition of water molecules [7][32]. Such challenge can be solved by using aqueous neutral electrolytes which proved to have higher potential window. For example, manganese dioxide is known to have good performances in aqueous neutral electrolytes than in alkaline and acidic medium [5]. Therefore, the maximum potential window of aqueous electrolytes in SC can be pushed way above 1.23 V by making use of asymmetric applications whereby different materials, are used as positive and negative electrodes with aqueous neutral electrolytes.

In this study, a straightforward and effectual way of complimenting the disadvantages of graphite (carbon-based material) and manganese dioxide by synthesis of composite through cost-effective hydrothermal process is reported. The composite was obtained through a separate synthesis of activated expanded graphite (AEG) and alpha-manganese dioxide (α-MnO_2). The synthesized electrode was characterised using structural, morphological and electrochemical

techniques. 1 M Na_2SO_4 was employed as an electrolyte to evaluate the electrochemical properties of the material in three- and two-electrode configurations. The optimized half-cell displayed the highest specific capacitance of 185.5 F g^{-1} at 1 A g^{-1} calculated from the galvanostatic charge-discharge (GCD) curve. Astoundingly, the highest specific energy of 33 Wh kg^{-1} with its corresponding specific power of 999 W kg^{-1} was obtained at 1 A g^{-1} in an operating potential window of 2.0 V in the assembled hybrid device using α-MnO_2/AEG composite as a positive electrode and AC-PVA as the negative electrode. This excellent electrochemical property proved the as-synthesized composite as a good electrode material for supercapacitor applications.

2. EXPERIMENTAL DETAILS

2.1 Preparation of alpha-manganese dioxide (α-MnO_2)

Alpha-manganese dioxide (α-MnO_2) was prepared by hydrothermal method using potassium per manganate powder ($KMnO_4$) [22]. A homogeneous mixture was produced by mixing 0.768 g $KMnO_4$ in 100 mL of deionised water (DI). Thereafter, 2 mL of hydrochloric acid (32 %) was added to the mixture drop wise upon magnetic stirring for 20 min to attain homogeneous solution. The solution was transferred to a Teflon lined autoclave for a duration time of 10 h under 150 ˚C hydrothermal temperature. Afterwards, the solution was removed and allowed to cool down to ambient temperature. The resulting mixture was decanted and washed several times using deionised water until a pH of 7 was reached. The brown precipitate was placed in the oven for 12 h at 80 ˚C.

2.2 Preparation of activated expanded graphite (AEG)

Activated expanded graphite (AEG) was synthesized as reported in our previous work [18]. Briefly, microwave oven was used to expand 5 g of graphite powder for 5 min with radiation power of 300 W. Thereafter, a mixture comprised of 1 g of activated expanded graphite (AEG) and 100 mL of 10 % wt polyvinylpyrrolidone (PVP) was sonicated for 12 h. Subsequently, 5 g of KOH was added to the mixture and stirred at 60 ˚C for 2 h. Thereafter, the precipitate obtained was dried for 12 h at 70 ˚C. The dried solid was positioned at the centre in a tube furnace and the temperature was steadily increased from ambient to 800 ˚C at 5 ˚C/min under a mixture of argon (300 sccm) and hydrogen gas (200 sccm), for carbonisation for 2 h. The expanded graphite (EG) changed into flakes-like carbon material through this procedure and denoted as activated expanded graphite (AEG). 1 M HCl was used to wash the black precipitate and further with deionised water, then finally it was dried in the oven at 60 ˚C for 12 h.

2.3 Preparation of α-MnO_2/AEG composite

100 mg of α-MnO_2 and 100 mg of AEG were mixed together into a crushing mortar and then crushed thoroughly until a homogeneous mixture was obtained. The mixture was positioned at the centre of a tube furnace and the temperature was steadily increased from ambient to 700 ˚C for 5 ˚C/min (for 2 h) under argon gas (200 sccm) to enable manganese and oxygen ions adsorbed onto the AEG material. The sample obtained was named as α-MnO_2/AEG composite.

2.4 Preparation of activated carbon-polyvinyl alcohol (AC-PVA)

First, 10 g of polyvinyl alcohol (PVA) was dissolved in 100 mL of DI water. The mixture was heated at 80 ˚C and then stirred for 2 h to produce 10 % wt PVA mixture. Thereafter, 100 mL of prepared 10 % wt PVA was sonicated for 30 min, after which 1.1 mL of 32 % HCl was added dropwise whilst stirring for 5 min to acquire a consistent mixture. The mixture obtained was transferred to an autoclave lined with Teflon and placed for 12 h in an oven at 180 ˚C. Resulting mixture was cooled to ambient temperature, filtered and then washed several times using DI water until neutral pH was obtained. The precipitate sample recovered was dried in the oven at 60 ˚C for 12 h. Thereafter, the powder sample was mixed with KOH (ratio of KOH and sample 4:1) and crush to a fine power in a mortal. The powder was transferred to the centre of a tube furnace and the temperature was steadily increased from ambient to 700 ˚C at 5 ˚C/min. The sample was kept at 700 ˚C for 2 h under argon gas in flow rate of 300 sccm before it cools down to room temperature. Thereafter, the derived activated carbon from PVA designated as AC-PVA was soaked in a mixture of 2 mL of HCl and 100 mL of DI water, and then thoroughly washed with DI water and dried at 60 ˚C overnight in ambient oven.

2.5 Characterization of the samples

The Zeiss Ultra Plus 55 field emission scanning electron microscopes (FE-SEM; Akishima-shi, Japan) run at 2.0 kV equipped with an energy-dispersive spectroscopy (EDS) and a JEOL-2100F high resolution transmission electron microscope (HRTEM FEI Tecnai-F30; Akishima-shi, Japan) functioned at 1.0 kV was acquired to analyse the as-synthesized sample morphology and elemental composition. Structural properties of the as-synthesized sample was analysed using X-ray

diffraction (XRD) analyser equipped in Bruker BV 2D PHASER Best Benchtop (PANalytical BV, Amsterdam, Netherland) controlled by a Cu *K*α$_1$ radiation source (λ= 0.15406 nm) at 30 mA and 50 kV through a reflection geometry of 2θ values (5 - 90˚) in a step size of 0.005˚. Further analysis to determine functional group was done in a range of 500 - 4000 cm^{-1} using FTIR spectroscopy. A WITec alpha 300 RAS+ Confocal micro-Raman microscope with 532 nm laser wavelength was utilized to analyze the degree of graphitization in the samples with a laser power and spectral acquisition time of 5 mW and 150 s, respectively on the sample to avoid sample heating. Nitrogen adsorption/desorption isotherms were measured by a NOVATOUCH with a quanta-chrome Touch-Win software analyzer. All samples were degassed at 100 ºC for 6 hours under high vacuum environments. The specific surface area was calculated with the Brunauer-Emmett-Teller (BET) method from the adsorption branch in the relative pressure range (P/Po) of 0.01 - 0.5 while the pore size distribution was determined using Barrett-Joyner-Halenda (BJH).

2.6 Electrochemical Characterization

The electrochemical evaluations were done in two- and three-electrode systems using EC-lab V1.40 software equipped within Biologic VMP300 potentiostat (Knoxville TN 37930, USA). A mixture of 10 % polyvinylidene fluoride (PVDF) used as a binder, 10 % of conductive carbon black and 80 % active material, were combined to prepare the working electrode. A homogeneous slurry mixture was formed by adding 1-methyl 2-pyrollidone (NMP) drops. Nickel foam was used as current collector (1.0 x 1.0 cm^2) in which the slurry was neatly pasted, then dried for 12 h at 60 ºC in the oven. Three electrode set-up was configured in 1 M Na_2SO_4 aqueous electrolyte using reference electrode (Ag/AgCl), glassy carbon (counter electrode) and as-synthesized sample

(working electrode). The cyclic voltammetry (CV) was measured within a potential window of 0.0 - 1.0 V vs Ag/AgCl at various scan rates from 10 - 100 mV s^{-1}. Specific currents range of 1 - 20 A g^{-1} in a potential window of 0.0 - 1.0 V was used for measuring galvanostatic charge-discharge (GCD). The specific capacitance (C_s) was evaluated from the GCD curve by applying Equation 1 as shown below [36]:

$$C_s = \frac{I_d \times \Delta t}{m \times \Delta V} \text{ [F g}^{-1}\text{]} \quad (1)$$

where, ΔV is the operating potential window in (V), I_d is the discharge current in (mA), m is the mass loading of the active material in (mg) and Δt (s) is the electrode discharge time.

The electrical resistance of the as-synthesized sample was estimated by using EIS Nyquist plot in an open circuit potential 0.0 V in a frequency range 10 mHz – 100 kHz. Columbic efficiency C_E (%) was determined as [1]:

$$C_E = \frac{t_D}{t_c} \times 100\ \% \quad (2)$$

were t_c and t_D are charging-discharging time at the same specific current respectively.

Two-electrode measurements were further used to investigate the performance of the fabricated device using α-MnO_2/AEG composite and AC-PVA as the positive and negative electrode, respectively. For a good working asymmetric device proper mass balance between the negative and the positive electrode has to be achieved through charge balancing using the equations below:

$$Q_+ = Q_- \quad (3)$$

where; Q_+ is a total positive charge and Q_- is a total negative charge. But, $Q = m \times C_s \times \Delta V$ and hence equation 3 above can be written as:

$$m_- \times \Delta V_- \times C_{s-} = m_+ \times \Delta V_+ \times C_{s+} \quad (4)$$

Equation (4) can further be reduced as shown below:

$$\frac{m_-}{m_+} = \frac{\Delta V_+ \times C_{s+}}{\Delta V_- \times C_{s-}} \quad (5)$$

where; ΔV_+ and ΔV_- are operating potential windows in a positive and negative electrodes, C_{s+} and C_{s-} are specific capacitances for positive and negative electrodes, and m_+ and m_- and masses for positive and negative electrodes, respectively.

The mass ratio of 1:2 was found using Eqn. 5, which resulted in a positive and negative electrodes masses of 2.2 and 3.8 mg, respectively, and making 6.0 mg/cm^2 as a total mass for α-MnO_2/AEG// AC-PVA device. The specific energy and specific power were estimated by utilizing Eqns. 6 and 7, respectively [11]:

$$E_d = \frac{I_d}{3.6} \int V dt \ \text{[Wh kg}^{-1}\text{]} \quad (6)$$

$$P_d = \frac{E_d}{\Delta t} \times 3600 \ \text{[W kg}^{-1}\text{]} \quad (7)$$

where, E_d present specific energy while P_d stand for specific power in their specified units.

3. RESULTS AND DISCUSSIONS

3.1 Morphology and structural analysis

Fig. 1 (a, b) displays SEM images at low and high magnification, respectively, for the as-synthesized α-MnO_2 sample. The figure shows rod-like nanostructure morphology which has also been observed by Yao et al. [37]. Fig. 1 (c, d) presents low and high magnification SEM images of the as-synthesized AEG sample showing an interconnected sheet-like flakes microstructure. The inter-connected porous nature of the AEG material is expected to allow good interaction of the electrolyte ions and improve the electrical conductivity of the α-MnO_2 during composite formation. This is expected to enhance the overall electrochemical performance of the composite material. Fig. 1 (e, f) shows low and high magnification SEM images of the sheet like morphology with agglomerated grains of rod-like nanostructures morphology for α-MnO_2/AEG composite sample. Furthermore, the addition of AEG into α-MnO_2 has changed the rod-like nanostructures into agglomerated grains of rod-like nanostructures as displayed in Fig. 1 (e, f). This was due to the chemical reaction of the mixture between α-MnO_2 and AEG, which increased surface energy of the composite material as expected to improve electrochemical performance.

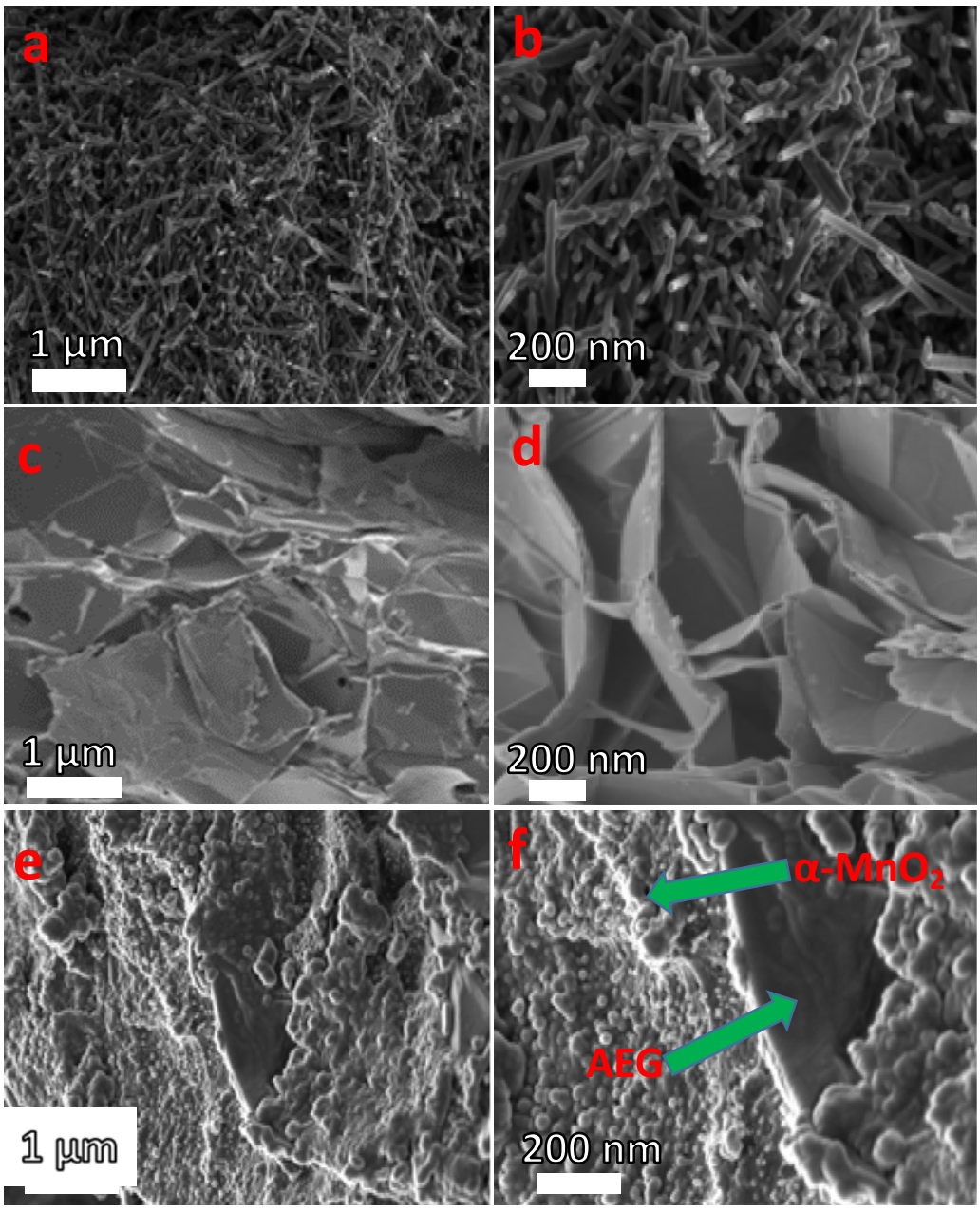

Fig. 1: (a, b), (c, d) and (e, f) are SEM images at low and high magnifications of α-MnO_2, AEG and α-MnO_2/AEG, respectively.

Fig. 2 (a, b and c) demonstrates the HRTEM images of α-MnO_2, AEG and α-MnO_2/AEG samples, respectively. The HRTEM confirmed the detailed morphology of the materials whereby Fig. 2 (a) shows rod-like morphology for α-MnO_2 while Fig. 2 (b) presents sheet like morphology for AEG and Fig. 2 (c) displays a mixture of α-MnO_2 and AEG morphology. The combination of sheet like morphology with agglomerated rod-like nanostructures indicates that α-MnO_2 is indeed loaded on AEG (Fig. 2 (c)). This is expected further to enhance the electrochemical performance of the composite sample. The elemental composition of the as-synthesized α-MnO_2/AEG composite was determined by EDS analysis. Fig. 2 (d) shows the EDS evaluation of α-MnO_2/AEG composite confirming the existence of Mn, O, C and K within the material. The presence of K in the spectrum of α-MnO_2/AEG composite is due to the potassium per manganate ($KMnO_4$) chemical utilized during synthesis of the material indicating that the sample was not completely washed to get rid of K. Furthermore, during sample preparation for EDS analysis, the Au-coating was applied which prove that the carbon present in the composite sample is not coming from the coating. Therefore, the presence of C in the α-MnO_2/AEG composite reveals that AEG was successfully loaded in the α-MnO_2 sample.

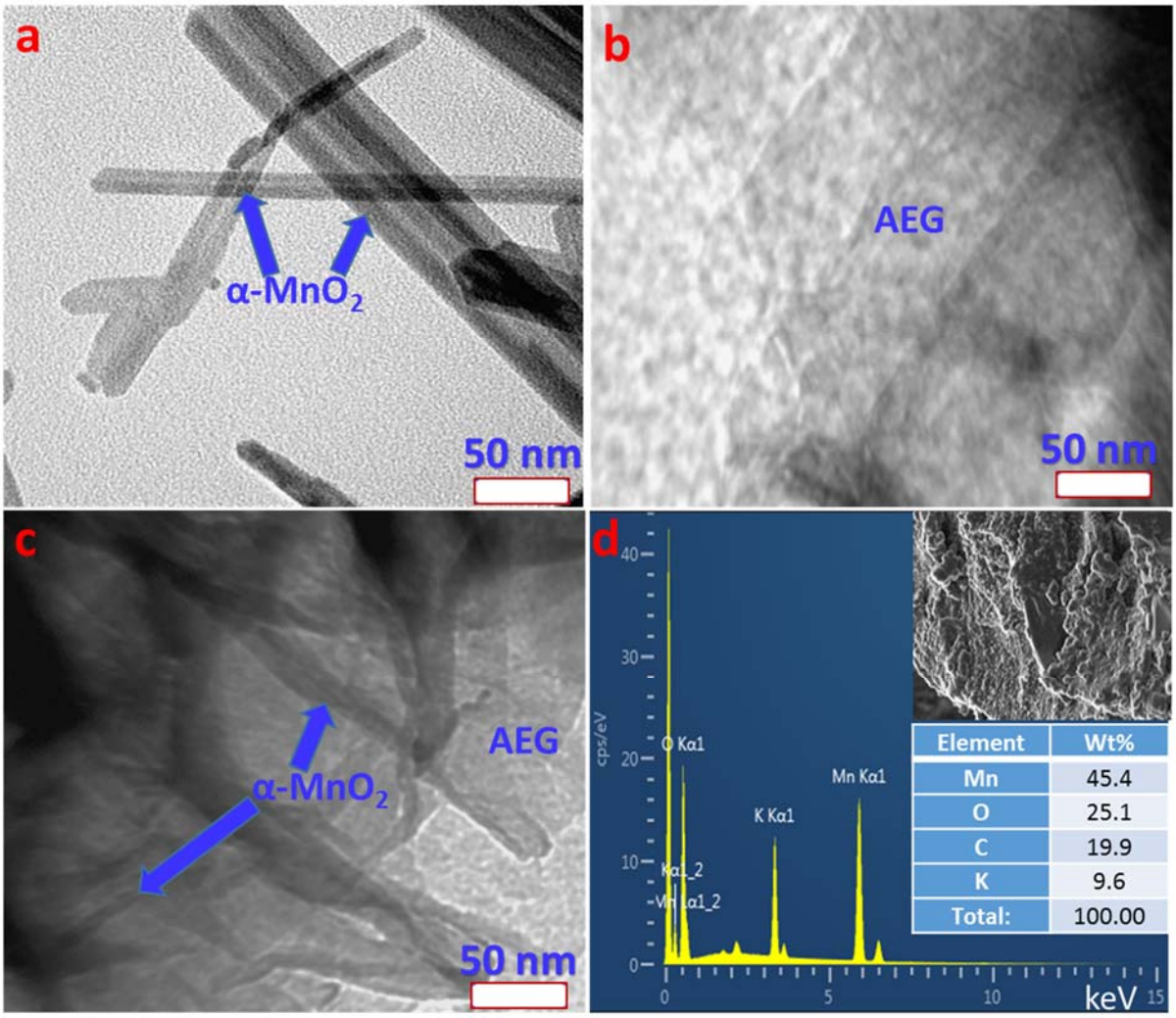

Fig. 2: (a), (b) and (c) are HRTEM images of α-MnO_2, AEG and α-MnO_2/AEG, respectively and (d) EDS analysis of α-MnO_2/AEG composite sample.

The nitrogen (N_2) gas adsorption and desorption analysis were done to measure the specific surface area and pore diameter of α-MnO_2 and α-MnO_2/AEG composite materials. Fig. 3 (a) and 3 (b) displays the N_2 adsorption/desorption isotherms and BJH pore size distribution, respectively of α-MnO_2 and α-MnO_2/AEG composite. Fig. 3 (a) shows the N_2 adsorption/desorption isotherms of α-MnO_2 and α-MnO_2/AEG composite whereby the specific surface area of α-MnO_2 was found to

increase due to the addition of AEG. The specific surface area noted for α-MnO_2 and α-MnO2/AEG composite was 31.284 m^2/g and 35.860 m^2/g, respectively. The improved specific surface area of the composite material can be attributed to the addition of AEG in the composite. As a result, this was reflected on the electrochemical performance of the composite. As shown in Fig. 3 (a) both α-MnO_2 and α-MnO_2/AEG present type-III behavior with an H3-type hysteresis loop with no saturation and showing the presence of mostly meso-poares.

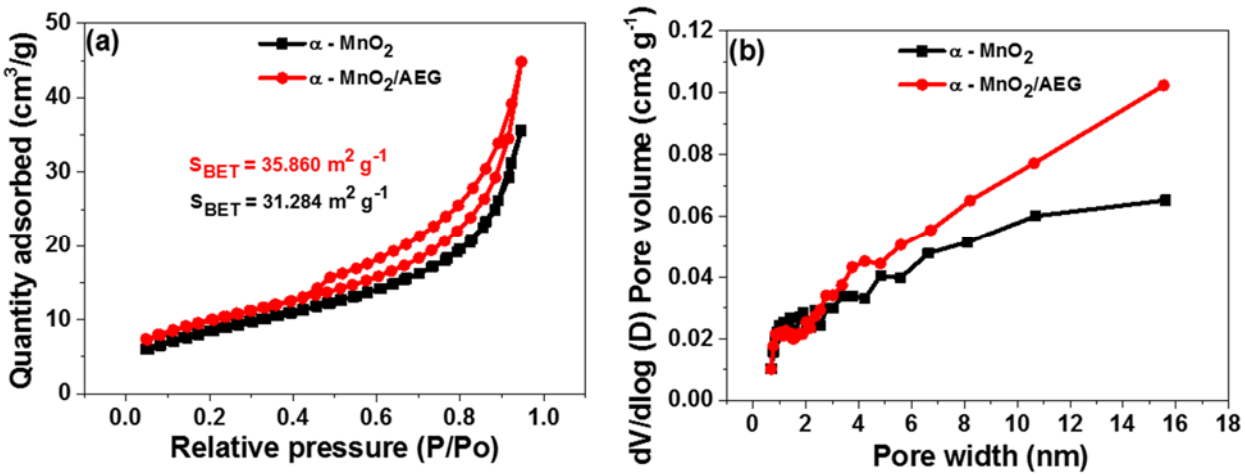

Fig. 3: (a) N_2 adsorption/desorption isotherms and (b) BJH pore size distributions of α-MnO_2 and α-MnO_2/AEG, respectively.

Fig. 4 (a) display XRD patterns for α-MnO_2, AEG and α-MnO_2/AEG in which the corresponding planes match with the XRD card no. JCPDS 44-0141 for MnO_2 and 96-900-0047 for AEG [18,38,39]. The diffraction peaks at 12.1^0 (110), 17.2^0 (200), 27.8^0 (310), 36.8^0 (211), 56.0^0 (600), 64.8^0 (002) and 71.8^0 (312) are signature peaks for alpha phase of α-MnO_2 while the peak at 10.2^0 (001), 26.5^0 (002), 40.1^0 (020), 44.0^0 (111), 54.6^0 (004) and 83.6^0 (200) correspond to AEG. The as-synthesized composite (α-MnO_2/AEG) spectrum indicates combination of diffraction peaks

from pristine (α-MnO_2) and AEG materials, which indicates that the materials didn't lose their crystallographic integrity during composite formation. The composite diffraction peaks show a slight shift which is due to changes in stoichiometric composition and the difference in ionic radii between the two materials [22,40]. Fig. 4 (b) displays FT-IR spectroscopy analysis of the as-synthesized α-MnO_2, AEG and α-MnO_2/AEG materials, respectively. It was noted that the =C-H bonds corresponds to the vibrations in the range of 675 - 1000 cm^{-1}. While vibrations in the range of 1050 - 1363 cm^{-1} are ascribed to O-H bonds which occur due to the interaction between carbon materials and Mn atoms. Hydrous MnO_2 is characterised by a vibration bands around 1593 cm^{-1} [41].

Raman spectroscopy is a non-destructive technique applied in this study to show the vibrational modes within the materials and degree of graphitization of the carbon present within the materials. Fig. 4 (c) demonstrates the Raman spectrum of AEG and α-MnO_2/AEG composite materials. The spectrum for AEG display the C-C stretching and double resonance transition mode of D, G and 2D picks corresponding to 1353 cm^{-1}, 1578 cm^{-1} and 2709 cm^{-1}, respectively [42]. For α-MnO_2/AEG composite G and 2D peaks are still observed with reduced intensity revealing the synergy effect caused by the interactivity between the two materials. Moreover, in this spectrum there was a sharp and strong peak around 647 cm^{-1} belonging to A_g spectroscopic species indicating a stretching vibration to the (Mn-O) of α-MnO_2 [43]. The well-defined appearance of this peak shows good crystallinity of α-MnO_2 in the composite sample. Furthermore, there is a presence of weak band of α-MnO_2 at 357 cm^{-1}. As observed in the XRD results of α-MnO_2/AEG composite, the presence of G and 2D peaks in the composite material confirm the presence of AEG.

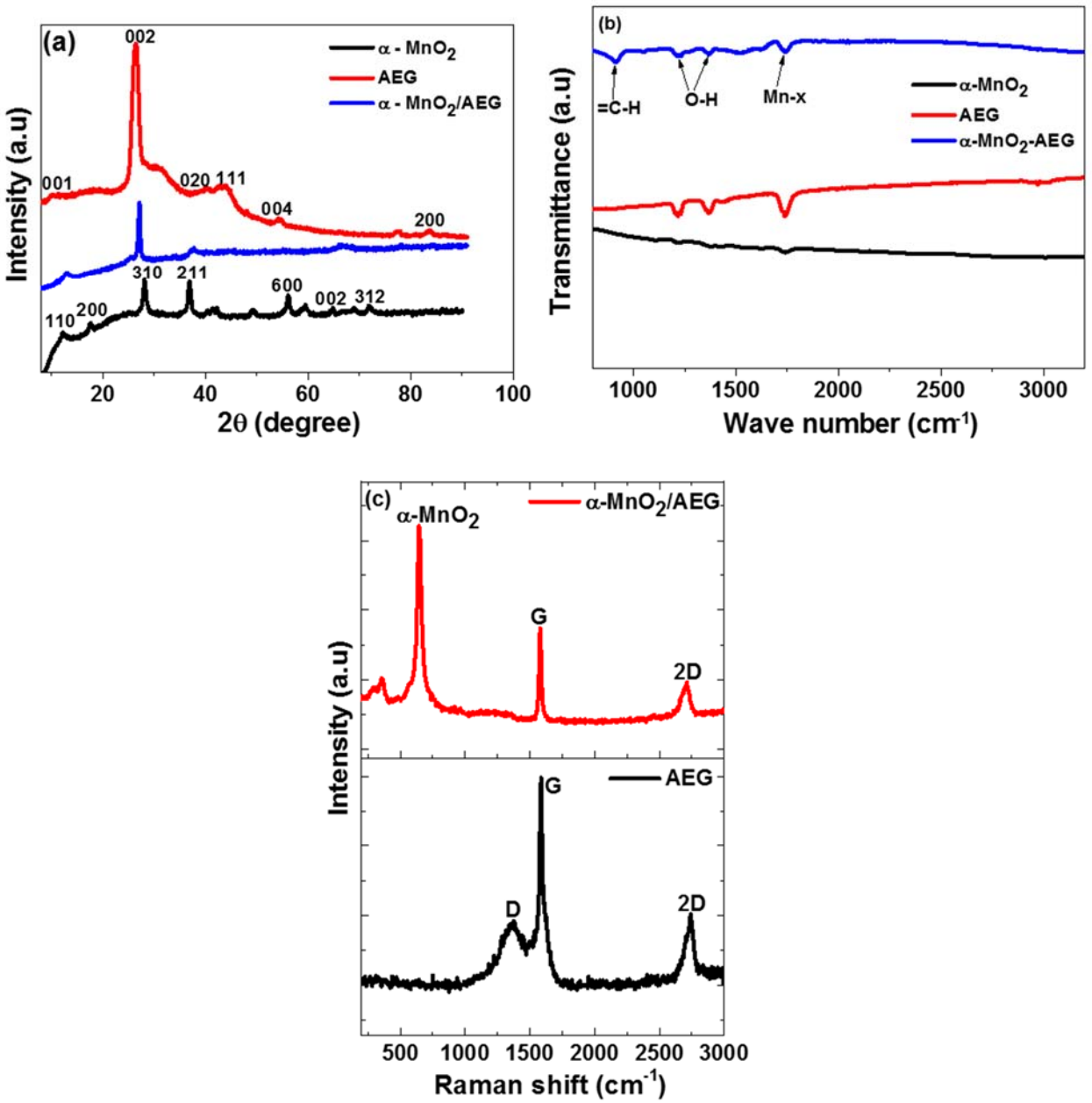

Fig. 4: (a) XRD, (b) FT-IR spectrum of α-MnO_2, AEG and α-MnO_2/AEG, and (c) Raman spectrum of AEG and α-MnO_2/AEG, respectively.

3.2 Electrochemical measurements

(i) Three electrode measurements

The cyclic voltammetry (CV) for α-MnO_2 was displayed in Fig. 5 (a) at different scan rates 10 – 100 mV s^{-1} in 1 M Na_2SO_4 electrolyte within a positive potential window ranging from 0.0 – 1.0 V vs Ag/AgCl. The CV has a quasi-rectangular shape which is an ideal behaviour for pseudocapacitive materials, such as transition metals like ruthenium oxide and nickel oxide [4][22][12]. A semi-linear shape displayed by the galvanostatic charge-discharge (GCD) in Fig. 5 (b) corresponds with the CV in Fig. 5 (a) for α-MnO_2 at various specific current range of 1 – 10 A g^{-1}. The specific capacitance of α-MnO_2 was calculated from the GCD curves using Eqn. 1 and found to be 132 F g^{-1} at 1 Ag^{-1}. The CV of AEG evaluated in 1 M Na_2SO_4 electrolyte in a positive potential window range 0.0 – 1.0 V vs Ag/AgCl, is shown in Fig. 5 (c) at various scan rates from 10 – 100 mV s^{-1}. The linear GCD curves of AEG at different specific current in a range of 1 – 10 A g^{-1} are shown in Fig. 5 (d) which confirms what was observed in Fig. 5 (c) which indicates that the AEG material has defined EDLC characteristics. This also indicates good capacitive behaviour of the material expected in carbon-based materials. The GCD curves were used to estimate the specific capacitance of AEG using Eqn. 1 as 153 F g^{-1} at 1 Ag^{-1}. As reported in our previous work, the high surface area of AEG contributed to the high specific capacitance [18].

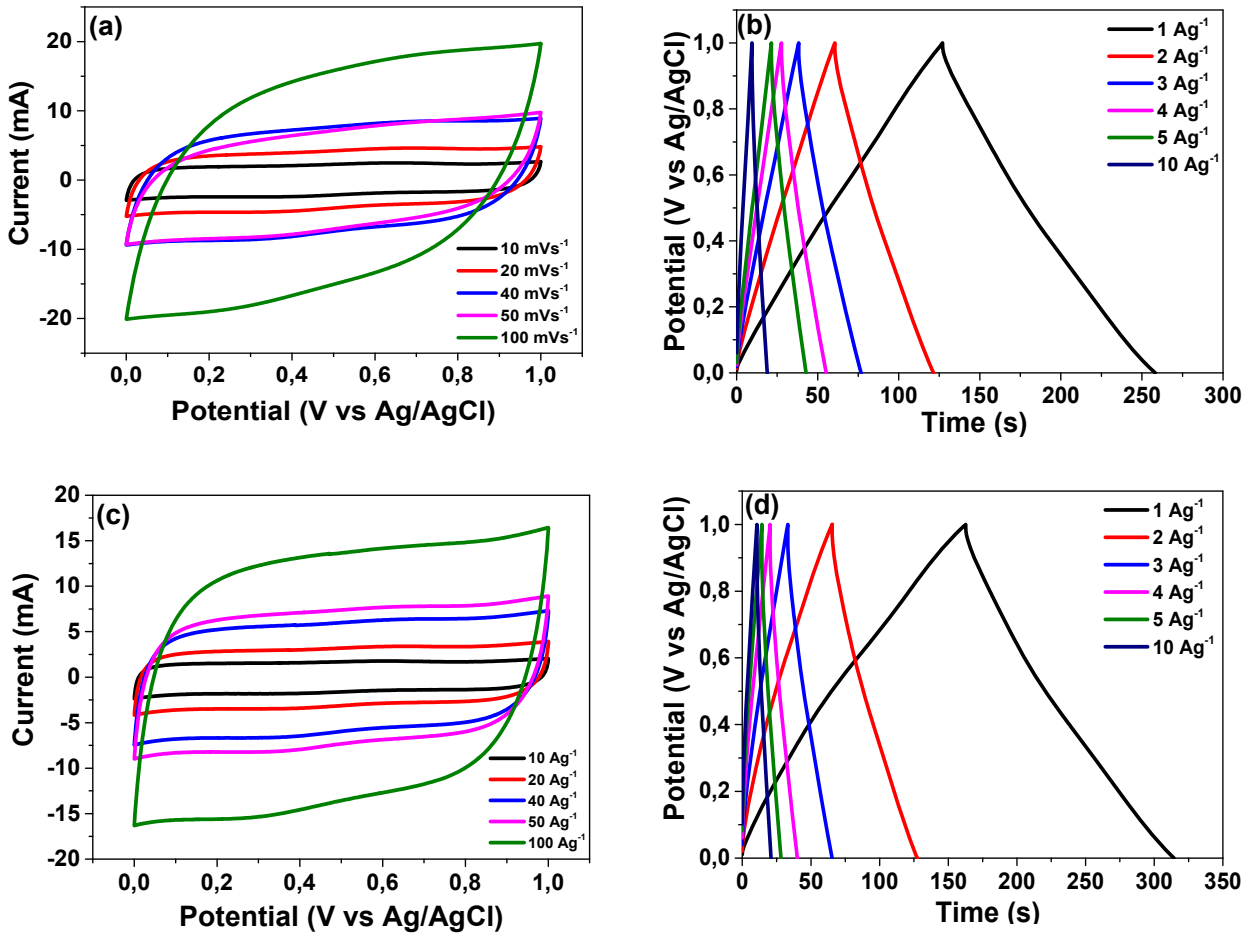

Fig. 5: (a, b) CV and GCD curves of α-MnO_2 and (c, d) CV and GCD curves of AEG in 1 M Na_2SO_4.

Fig. 6 (a and b) represent the electrochemical measurements of α-MnO_2/AEG composite conducted using 1 M Na_2SO_4 electrolyte. The CV curves performed at various scan rates from 10 – 100 mV s^{-1} within a positive potential window range of 0.0 – 1.1 V vs Ag/AgCl is displayed in Fig. 6 (a) indicating traces of pseudocapacitive behaviour which attributed to α-MnO_2 in the composite. The quasi-rectangular shape of the CV also indicates oxidation or reduction responses arising on the surface of the electrode and electrolyte. Fig. 6 (b) indicates linear GCD curves at various specific current in a range of 1 to 10 A g^{-1} displaying EDLC features as observed in Fig. 6

(a) of the CV curves. The synergy effect of the combined α-MnO2 and AEG material was noticed by the increase in potential window of the composite material, increase in the discharge time of the GCD curves and, increase in the current response of the CV curves compared to single constituents. Specific capacitance of α-MnO_2/AEG composite evaluated using Eqn. 1 was estimated to be 185.5 F g^{-1} which is superior to132 and 153 F g^{-1} for α-MnO_2 and AEG at 1 Ag^{-1}, respectively. This improved performance is due to the synergy between α-MnO_2 which has high diffusion rate and ability to store large size cations and AEG which has high conductivity and hence resulted into high specific capacitance of the composite material [32]. Fig. 6 (c) demonstrates specific capacitances versus specific current for α-MnO_2, AEG and α-MnO_2/AEG composite which shows a steady decrease in specific capacitances with increase in specific currents. The specific capacitance of the composite is still higher than those of the presitine samples throughout. Subsequently, the α-MnO2, AEG and α-MnO2/AEG conserved about 58 %, 61 % and 64 % rate capability, respectively. This is associated with the redox reaction occurring on a surface which may result in change of oxidation state of manganese [24]. Moreover, EIS was performed to access the capacitive performance of the as-synthesized α-MnO_2/AEG composite material. Fig. 6 (d) indicates EIS Nyquist plot for α-MnO_2, AEG and α-MnO_2/AEG composite measured at a frequency range 10 mHz – 100 kHz. The equivalent series resistance (ESR) value was estimated at a high-frequency region as presented in an inset to Fig. 6 (d). The value was achieved, by reading the data of the intercept to the x-axis of the real component (Z') curve. The equivalent series resistance (ESR) values of 1.8, 3.1 and 1.6 Ω were recorded for α-MnO2, AEG and α-MnO2/AEG, respectively. The ESR value for α-MnO_2/AEG shows an improvement in the electrolytic ions diffusion resistance in a composite compared to α-MnO_2 and AEG. Furthermore, α-MnO_2/AEG composite has shortest diffusion length compared to α-MnO_2 and AEG which

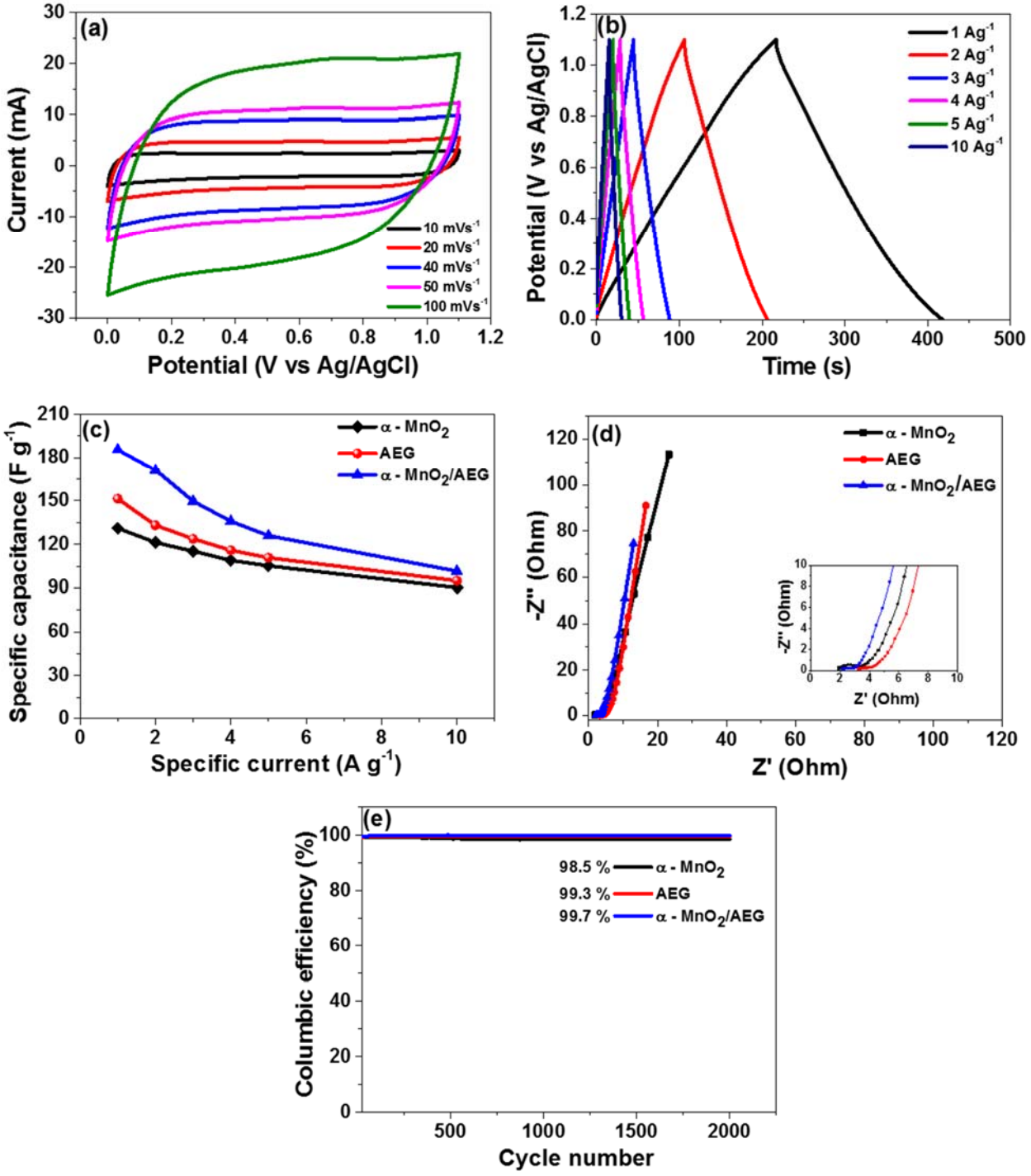

Fig. 6: (a) CV curves and (b) GCD curves for α-MnO_2/AEG in 1 M Na_2SO_4, (c) specific capacitance versus specific current, (d) EIS Nyquist plot and (e) cycling performance for α-MnO_2, AEG and α-MnO_2 /AEG, respectively in 1 M Na_2SO_4.

signify the good synergy between α-MnO_2 and AEG. Additional analysis was done using columbic efficiency versus cycle number at 5 A g^{-1} for up to 2000 charge-discharge cycles for α-MnO_2, AEG and α-MnO_2/AEG, respectively (Fig. 6 (e)). Columbic efficiency evaluated using Eqn. 2 was found to be 98.5 %, 99.3 % and 99.7 % for α-MnO_2, AEG and α-MnO_2/AEG, respectively. The results show that α-MnO_2/AEG composite has superior cycling stability of approximately 100 % compared to α-MnO_2 and AEG. This can be attributed to the increase in conductivity of α-MnO_2 due to the presence of carbon material (AEG) [5].

(ii) Two electrode measurements

The electrochemical measurements of α-MnO_2/AEG composite and AC-PVA as positive and negative electrodes, respectively, in 1 M Na_2SO_4 electrolyte are displayed in Fig. 7. Fig. 7 (a) displays the CV curves at a scan rate of 50 mV s^{-1} for α-MnO_2/AEG and AC-PVA in a positive and negative potential windows of 0.0 to 1.1 and -0.9 to 0.0 V vs Ag/AgCl, respectively. The AC-PVA shows more resistive behavior due to the presence of some functional groups which makes the electrode to show pseudocapacitive behavior while α-MnO_2/AEG shows much better CV resembling an EDLC behavior indicating good capacitive properties of the material [22]. The GCD curves for α-MnO_2/AEG composite and AC-PVA at 1 A g^{-1} is shown in Fig. 7 (b) confirming what was observed in Fig. 7 (a). A further detailed study of AC-PVA is ongoing and shall be discussed in another publication.

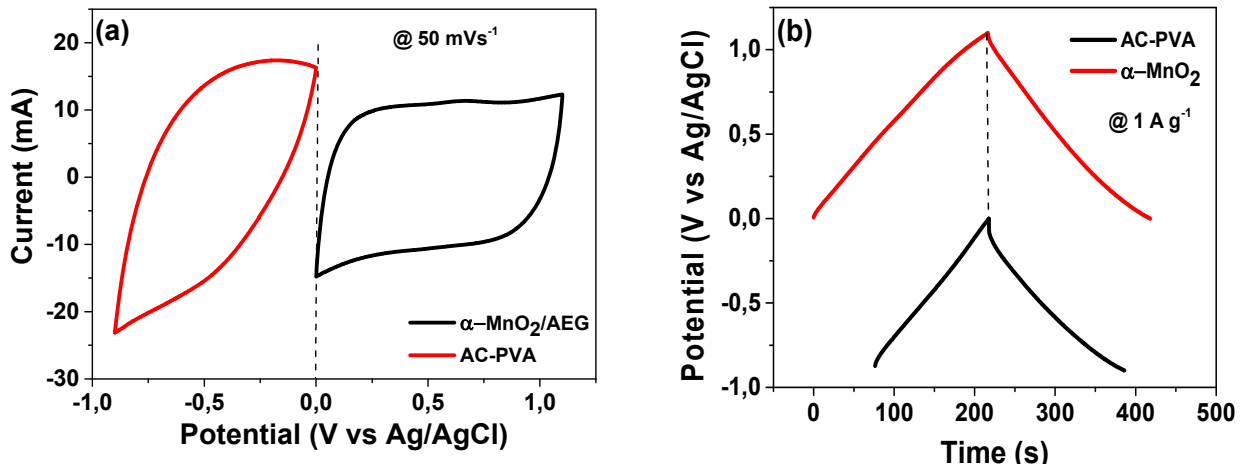

Fig. 7: (a) CV curves at 50 mV s^{-1} and (b) GCD curves at 1 A g^{-1} for AC-PVA and α-MnO_2 /AEG in 1 M Na_2SO_4.

The α-MnO_2/AEG composite material was further investigated using two-electrode measurements for practical applications. The assembled device employing α-MnO_2/AEG composite and AC-PVA as positive and negative electrodes, respectively, was abbreviated as α-MnO_2/AEG//AC-PVA asymmetric device. Fig. 8 (a) displays CV curves at various scan rates ranging from 10 - 100 mV s^{-1} for α-MnO_2/AEG//AC-PVA asymmetric device within a potential window range of 0.0 – 2.0 V. The CV curves show quasi rectangular shape without redox peaks signifying the occurrence of adsorption and desorption activities of electrolyte ions at the interface of the electrolyte and electrode. A semi-linear GCD curve in Fig. 8 (b) indicates a pseudocapacitive nature of the device confirming what was observed in Fig. 8 (a). The specific capacitance of α-MnO_2/AEG//AC-PVA asymmetric device was calculated using Eqn. 1 and estimated to be 59.4 F g^{-1} at 1 Ag^{-1}. Fig. 8 (c) displays specific capacitance versus specific current of α-MnO_2/AEG//AC-PVA asymmetric device. It was noted that there is a steady decrease in specific capacitance with an increase in specific current which is attributed to the synergy between α-MnO_2/AEG and AC-PVA which

allow electrolyte ions to interact with the material and hence prevent rapid reduction of the capacitance. This proves high rate capability of the α-MnO_2/AEG//AC-PVA asymmetric device of 58 % [44]. Fig. 8 (d) shows a Ragone plot displaying specific energy versus specific power for α-MnO_2/AEG//AC-PVA asymmetric device evaluated using Eqns. 6 and 7. The α-MnO_2/AEG//AC-PVA asymmetric device at 1 A g^{-1}, recorded the highest specific energy with its corresponding specific power of 33 Wh k g^{-1} and 999 W kg^{-1}, respectively evaluated from the GCD curve. The electrochemical measurements of the assembled α-MnO_2/AEG//AC-PVA asymmetric device, in comparison with previous similar work published, is illustrated in Table 1 below whereby the specific energy reported here is comparable or higher than those in the literature. This achievement is attributed to the structural integrity of α-MnO_2/AEG composite where the tunnels of α-MnO_2 are theoretically large [28]. Furthermore, large surface area of AEG (457 m^2 g^{-1}) [42] which has more active sites for redox reaction and large opening pores that allows interaction of Na^+ cations to pass through contributed to the better performance of the device.

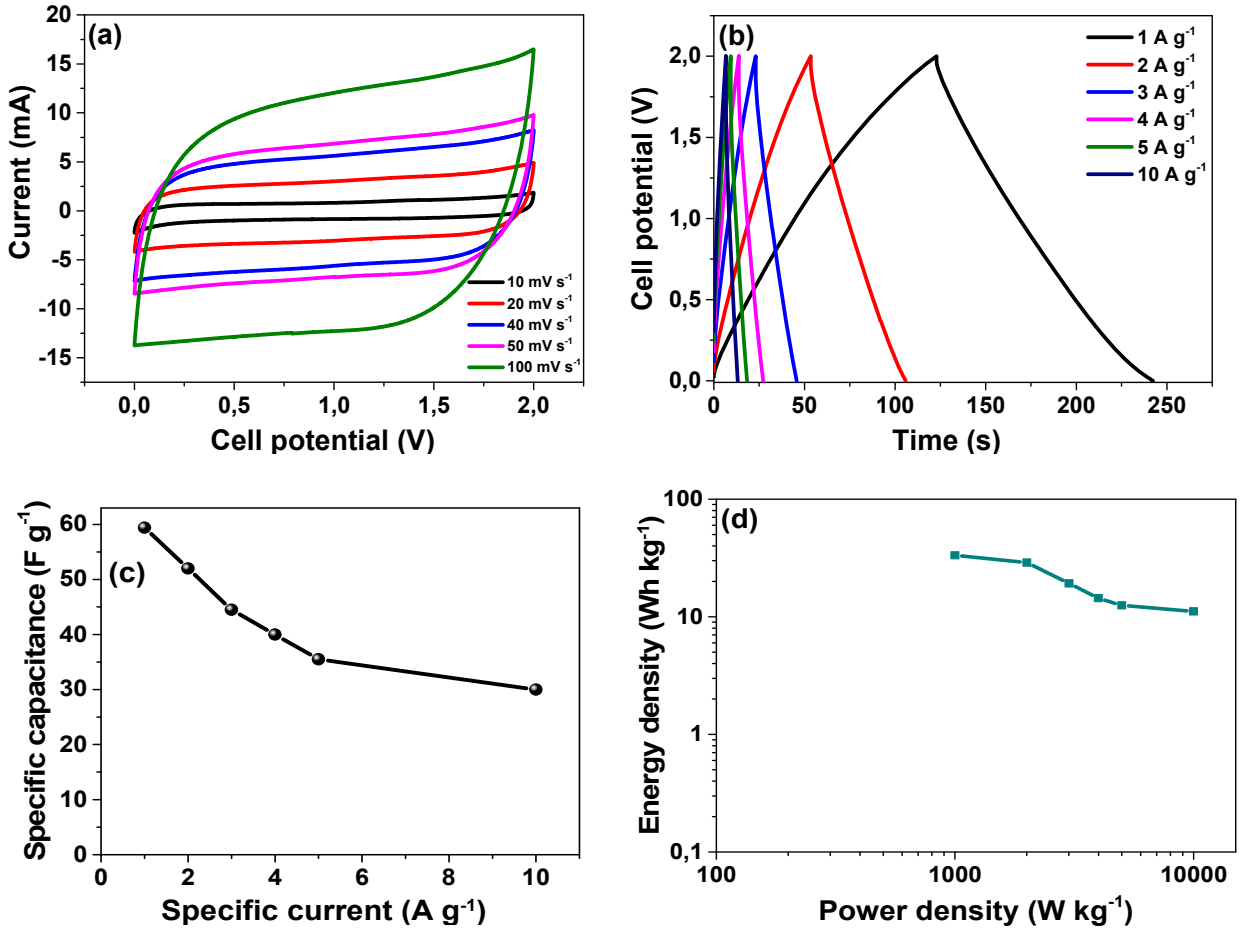

Fig. 8: (a) CV curves at different scan rates, (b) GCD curves at different specific currents, (c) specific capacitance versus specific current and (d) Ragone plot for α-MnO_2/AEG//AC-PVA asymmetric device in 1 M Na_2SO_4, respectively.

Table 1: Comparisons of electrochemical measurements of various devices from the literature with similar material evaluated in two-electrode measurements.

Electrode (Device material)	Electrolyte	Potential window (V)	Specific energy (Wh kg^{-1})	Specific power (W kg^{-1})	Ref. No.
MnO_2//AC	1 M Na_2SO_4	2.0	17.1	100	[11]
MnO_2/CNT//AC	2 M KNO_3	2.0	21	123 000	[45]
MnO_2-CNT//AC	1 M Li_2SO_4	2.0	25	500	[5]
MnO_2 nanotubes//AC	1 M Na_2SO4	1.8	22.5	146 200	[46]
MnO_2-AEG//AC-PVA	**1 M Na_2SO_4**	**2.0**	**33**	**999**	**This Work**

Fig. 9 (a) indicates long cycling performance at 5 A g^{-1} conducted for up to 10, 000 cycles to evaluate the stability of α-MnO_2/AEG//AC-PVA asymmetric device. The assembled α-MnO_2/AEG//AC-PVA asymmetric device confirmed a columbic efficiency of 99.8 % throughout 10, 000 cycles. The cycling performance is vital indicating stability of the device over a long charge/discharge due to good redox reaction that occurs between α-MnO_2 and AEG. This indicates that the as-synthesized α-MnO_2/AEG composite has stable chemical structure resulting from Mn^{2+} oxidation state which can withstand charge and discharge over a prolonged period [5]. Fig. 9 (b) shows the durability of the device using α-MnO_2/AEG//AC-PVA after performing a voltage holding with a floating time of up to 70 h. At 5 A g^{-1}, the specific capacitance versus floating time of up to 70 h for α-MnO_2/AEG//AC-PVA asymmetric device exposed to a maximum voltage of

2.0 V was achieved. The specific capacitance of the device was evaluated after being subjected to the charge-discharge for three cycles. The device was held at 5 A g^{-1} for 10 h at the highest potential of 2.0 V, then subjected to another charge-discharge process. The process was repeated for up to 70 h. The specific capacitance increased in the first 10 h but later became stable from 10 h for over 70 h of the test. This could be due to the fact that at initial stage the electrode lacks wettability. Thus, the device displayed about 70 % of its initial capacitance after 70 h. EIS Nyquist plot for α-MnO_2/AEG//AC-PVA asymmetric device was performed before and after stability as shown in Fig. 9 (c). The results show an improvement in performance of the device after stability, however, there is a small deviation of the curve away from y-axis after stability as compared to the one before stability. The improvement in the diffusion length and equivalent series resistance from 2.3 to 1.8 Ω before and after stability was noted. This shows an improvement in wettability which allows the material to access more ions when the device is exposed to many cycles. Fig. 9 (d) indicates the phase angle versus frequency curve presenting the phase angle of about -78.5º which is closer to the ideal value of -90º denoting that, α-MnO_2/AEG//AC-PVA asymmetric device is approaching to the ideal capacitive performance.

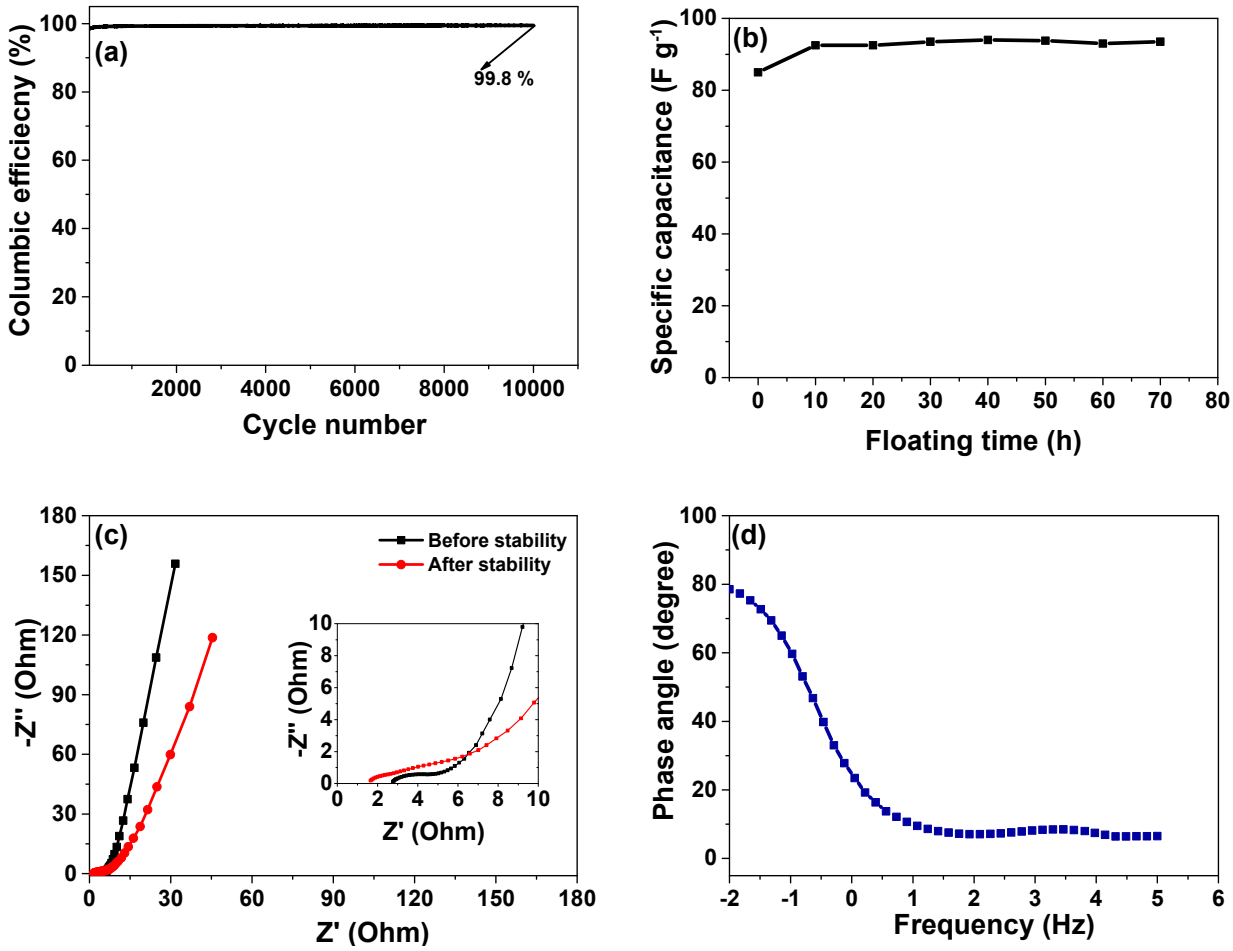

Fig. 9: (a) Cycling performance, (b) floating time versus specific capacitance, (c) EIS Nyquist plot before and after cycling and (d) frequency versus phase angle for α-MnO_2 /AEG//AC-PVA asymmetric device in 1 M Na_2SO_4, respectively.

4. Conclusion

Alpha-manganese dioxide/activated expanded graphite (α-MnO_2/AEG) was successfully synthesized via simple hydrothermal method. The as-synthesized hybrid material displayed a sheet like morphology with agglomerated grains of rod-like nanostructures morphology. The specific capacitance of about 185.5 F g^{-1} was recorded in 1 M Na_2SO_4 for the half-cell at 1 A g^{-1}. At 5 A g^{-1}, the material was able to display a cycling performance of 99.7 % for the half-cell over 2000 cycles. The as-synthesized α-MnO_2/AEG composite and AC-PVA were used as positive and

negative electrodes, respectively to assemble α-MnO_2/AEG//AC-PVA hybrid device. The device showed great electrochemical behaviour at 1 A g^{-1} within the maximum potential window of 2.0 V, which gave the highest specific energy and specific power of 33 Wh kg^{-1} and 999 W kg^{-1}, respectively. Stability of the device was done at 5 A g^{-1} by performing a columbic efficiency versus cycle number which revealed an efficiency of 99.8 % after 10, 000 cycles. Stability of the device was further confirmed by subjecting a device to a voltage holding with a floating time of up to 70 h at 5 A g^{-1}. These results demonstrated that the studied materials are of great potential for supercapacitor applications.

ACKNOWLEDGEMENTS

This work was supported by South African Research Chairs Initiative of the Department of Science and Technology and National Research Foundation of South Africa (Grant No. 61056) any opinion, finding and conclusion expressed in this material are that of the authors, and the NRF does not accept any liability in this regard. Phathutshedzo Murovhi acknowledges the financial support from NRF through SARChI chair in Carbon Technology and Materials.

REFERRENCES

[1] D.J. Tarimo, K.O. Oyedotun, A.A. Mirghni, N. Manyala, Sulphur-reduced graphene oxide composite with improved electrochemical performance for supercapacitor applications, International Journal of Hydrogen Energy. (2020). https://doi.org/10.1016/j.ijhydene.2020.03.059.

[2] G.Z. Chen, Supercapacitor and supercapattery as emerging electrochemical energy stores, International Materials Reviews. 62 (2017) 173–202. https://doi.org/10.1080/09506608.2016.1240914.

[3] C. Wu, S. Gu, Q. Zhang, Y. Bai, M. Li, Y. Yuan, H. Wang, X. Liu, Y. Yuan, N. Zhu, F. Wu, H. Li, L. Gu, J. Lu, Electrochemically activated spinel manganese oxide for rechargeable aqueous aluminum battery, Nature Communications. 10 (2019) 1–10. https://doi.org/10.1038/s41467-018-07980-7.

[4] A. González, E. Goikolea, J.A. Barrena, R. Mysyk, Review on supercapacitors: Technologies and materials, Renewable and Sustainable Energy Reviews. 58 (2016) 1189–1206. https://doi.org/10.1016/j.rser.2015.12.249.

[5] F. Ochai-Ejeh, M.J. Madito, K. Makgopa, M.N. Rantho, O. Olaniyan, N. Manyala, Electrochemical performance of hybrid supercapacitor device based on birnessite-type manganese oxide decorated on uncapped carbon nanotubes and porous activated carbon nanostructures, Electrochimica Acta. 289 (2018) 363–375. https://doi.org/10.1016/j.electacta.2018.09.032.

[6] L. Li, Z.A. Hu, N. An, Y.Y. Yang, Z.M. Li, H.Y. Wu, Facile synthesis of MnO2/CNTs composite for supercapacitor electrodes with long cycle stability, Journal of Physical Chemistry C. 118 (2014) 22865–22872. https://doi.org/10.1021/jp505744p.

[7] L. Demarconnay, E. Raymundo-Piñero, F. Béguin, Adjustment of electrodes potential window in an asymmetric carbon/MnO 2 supercapacitor, Journal of Power Sources. 196 (2011) 580–586. https://doi.org/10.1016/j.jpowsour.2010.06.013.

[8] F.O. Ochai-Ejeh, M.J. Madito, D.Y. Momodu, A.A. Khaleed, O. Olaniyan, N. Manyala, High performance hybrid supercapacitor device based on cobalt manganese layered

double hydroxide and activated carbon derived from cork (Quercus Suber), Electrochimica Acta. 252 (2017) 41–54. https://doi.org/10.1016/j.electacta.2017.08.163.

[9] M. Liang, L. Zhi, Graphene-based electrode materials for rechargeable lithium batteries, Journal of Materials Chemistry. 19 (2009) 5871–5878. https://doi.org/10.1039/b901551e.

[10] J.K. Gan, Y.S. Lim, A. Pandikumar, N.M. Huang, H.N. Lim, Graphene/polypyrrole-coated carbon nanofiber core-shell architecture electrode for electrochemical capacitors, RSC Advances. 5 (2015) 12692–12699. https://doi.org/10.1039/c4ra14922j.

[11] X. Zhang, P. Yu, H. Zhang, D. Zhang, X. Sun, Y. Ma, Rapid hydrothermal synthesis of hierarchical nanostructures assembled from ultrathin birnessite-type MnO2 nanosheets for supercapacitor applications, Electrochimica Acta. 89 (2013) 523–529. https://doi.org/10.1016/j.electacta.2012.11.089.

[12] J. Yan, T. Wei, J. Cheng, Z. Fan, M. Zhang, Preparation and electrochemical properties of lamellar MnO2 for supercapacitors, Materials Research Bulletin. 45 (2010) 210–215. https://doi.org/10.1016/j.materresbull.2009.09.016.

[13] X. Ge, F. Tian, Z. Wu, Y. Yan, G. Cravotto, Z. Wu, Adsorption of naphthalene from aqueous solution on coal-based activated carbon modified by microwave induction: Microwave power effects, Chemical Engineering and Processing: Process Intensification. 91 (2015) 67–77. https://doi.org/10.1016/j.cep.2015.03.019.

[14] B. Acevedo, C. Barriocanal, I. Lupul, G. Gryglewicz, Properties and performance of mesoporous activated carbons from scrap tyres, bituminous wastes and coal, Fuel. 151 (2015) 83–90. https://doi.org/10.1016/j.fuel.2015.01.010.

[15] I.I. Salame, T.J. Bandosz, Surface chemistry of activated carbons: Combining the results of temperature-programmed desorption, Boehm, and potentiometric titrations, Journal of

Colloid and Interface Science. 240 (2001) 252–258. https://doi.org/10.1006/jcis.2001.7596.

[16] W. Chen, H. Zhang, Y. Huang, W. Wang, A fish scale based hierarchical lamellar porous carbon material obtained using a natural template for high performance electrochemical capacitors, Journal of Materials Chemistry. 20 (2010) 4773–4775. https://doi.org/10.1039/c0jm00382d.

[17] T.E. Rufford, D. Hulicova-Jurcakova, Z. Zhu, G.Q. Lu, Nanoporous carbon electrode from waste coffee beans for high performance supercapacitors, Electrochemistry Communications. 10 (2008) 1594–1597. https://doi.org/10.1016/j.elecom.2008.08.022.

[18] F. Barzegar, A. Bello, J.K. Dangbegnon, N. Manyala, X. Xia, Asymmetric supercapacitor based on activated expanded graphite and pinecone tree activated carbon with excellent stability, Applied Energy. 207 (2017) 417–426. https://doi.org/10.1016/j.apenergy.2017.05.110.

[19] J. Jiang, A. Kucernak, Electrochemical supercapacitor material based on manganese oxide: Preparation and characterization, Electrochimica Acta. 47 (2002) 2381–2386. https://doi.org/10.1016/S0013-4686(02)00031-2.

[20] C. Yu, R. Chen, J.J. Li, J.J. Li, M. Drahansky, M.. Paridah, A. Moradbak, A.. Mohamed, H. abdulwahab taiwo Owolabi, FolaLi, M. Asniza, S.H.. Abdul Khalid, T. Sharma, N. Dohare, M. Kumari, U.K. Singh, A.B. Khan, M.S. Borse, R. Patel, A. Paez, A. Howe, D. Goldschmidt, C. Corporation, J. Coates, F. Reading, We are IntechOpen , the world ' s leading publisher of Open Access books Built by scientists , for scientists TOP 1 %, Intech. (2012) 13. https://doi.org/10.1016/j.colsurfa.2011.12.014.

[21] P.B. Tarigan, 済無No Title No Title, Journal of Chemical Information and Modeling. 53

(2013) 1689–1699. https://doi.org/10.1017/CBO9781107415324.004.

[22] X. Zhao, Y. Hou, Y. Wang, L. Yang, L. Zhu, R. Cao, Z. Sha, Prepared MnO2 with different crystal forms as electrode materials for supercapacitors: Experimental research from hydrothermal crystallization process to electrochemical performances, RSC Advances. 7 (2017) 40286–40294. https://doi.org/10.1039/c7ra06369e.

[23] R.A. Aziz, R. Jose, Charge storage capability of tunnel MnO2 and alkaline layered Na-MnO2 as anode material for aqueous asymmetry supercapacitor, Journal of Electroanalytical Chemistry. 799 (2017) 538–546. https://doi.org/10.1016/j.jelechem.2017.06.014.

[24] Z. Pan, Y. Qiu, J. Yang, F. Ye, Y. Xu, X. Zhang, M. Liu, Y. Zhang, Ultra-endurance flexible all-solid-state asymmetric supercapacitors based on three-dimensionally coated MnOx nanosheets on nanoporous current collectors, Nano Energy. 26 (2016) 610–619. https://doi.org/10.1016/j.nanoen.2016.05.053.

[25] W. Wei, X. Cui, W. Chen, D.G. Ivey, Manganese oxide-based materials as electrochemical supercapacitor electrodes, Chemical Society Reviews. 40 (2011) 1697–1721. https://doi.org/10.1039/c0cs00127a.

[26] S. Li, Y. Chang, G. Han, H. Song, Y. Chang, Y. Xiao, Asymmetric supercapacitor based on reduced graphene oxide/MnO 2 and polypyrrole deposited on carbon foam derived from melamine sponge, Journal of Physics and Chemistry of Solids. 130 (2019) 100–110. https://doi.org/10.1016/j.jpcs.2019.02.020.

[27] S. Zhang, N. Pan, Supercapacitors performance evaluation, Advanced Energy Materials. 5 (2015) 1–19. https://doi.org/10.1002/aenm.201401401.

[28] Y. Li, Z. Xu, D. Wang, J. Zhao, H. Zhang, Snowflake-like core-shell α-MnO2@δ-MnO2

for high performance asymmetric supercapacitor, Electrochimica Acta. 251 (2017) 344–354. https://doi.org/10.1016/j.electacta.2017.08.146.

[29] J. Yan, Z. Fan, T. Wei, W. Qian, M. Zhang, F. Wei, Fast and reversible surface redox reaction of graphene-MnO2 composites as supercapacitor electrodes, Carbon. 48 (2010) 3825–3833. https://doi.org/10.1016/j.carbon.2010.06.047.

[30] R. Kumar, B.K. Singh, A. Soam, S. Parida, P. Bhargava, In-situ carbon coated manganese oxide nanorods (ISCC-MnO 2 NRs) as an electrode material for supercapacitors, Diamond and Related Materials. 94 (2019) 110–117. https://doi.org/10.1016/j.diamond.2019.03.003.

[31] Y. Li, D. Cao, Y. Wang, S. Yang, D. Zhang, K. Ye, K. Cheng, J. Yin, G. Wang, Y. Xu, Hydrothermal deposition of manganese dioxide nanosheets on electrodeposited graphene covered nickel foam as a high-performance electrode for supercapacitors, Journal of Power Sources. 279 (2015) 138–145. https://doi.org/10.1016/j.jpowsour.2014.12.153.

[32] Y. Shao, M.F. El-Kady, J. Sun, Y. Li, Q. Zhang, M. Zhu, H. Wang, B. Dunn, R.B. Kaner, Design and Mechanisms of Asymmetric Supercapacitors, Chemical Reviews. 118 (2018) 9233–9280. https://doi.org/10.1021/acs.chemrev.8b00252.

[33] S.M. Li, Y.S. Wang, S.Y. Yang, C.H. Liu, K.H. Chang, H.W. Tien, N.T. Wen, C.C.M. Ma, C.C. Hu, Electrochemical deposition of nanostructured manganese oxide on hierarchically porous graphene-carbon nanotube structure for ultrahigh-performance electrochemical capacitors, Journal of Power Sources. 225 (2013) 347–355. https://doi.org/10.1016/j.jpowsour.2012.10.037.

[34] X. Su, L. Yu, G. Cheng, H. Zhang, M. Sun, X. Zhang, High-performance α-MnO2 nanowire electrode for supercapacitors, Applied Energy. 153 (2015) 94–100.

https://doi.org/10.1016/j.apenergy.2014.07.094.

[35] B. Wang, J. Qiu, H. Feng, N. Wang, E. Sakai, T. Komiyama, Preparation of MnO2/carbon nanowires composites for supercapacitors, Electrochimica Acta. 212 (2016) 710–721. https://doi.org/10.1016/j.electacta.2016.07.066.

[36] H. Lv, Y. Yuan, Q. Xu, H. Liu, Y.G. Wang, Y. Xia, Carbon quantum dots anchoring MnO2/graphene aerogel exhibits excellent performance as electrode materials for supercapacitor, Journal of Power Sources. 398 (2018) 167–174. https://doi.org/10.1016/j.jpowsour.2018.07.059.

[37] W. Yao, J. Wang, H. Li, Y. Lu, Flexible α-MnO2 paper formed by millimeter-long nanowires for supercapacitor electrodes, Journal of Power Sources. 247 (2014) 824–830. https://doi.org/10.1016/j.jpowsour.2013.09.039.

[38] P.M. Shafi, R. Dhanabal, A. Chithambararaj, S. Velmathi, A.C. Bose, α-MnO2/h-MoO3 Hybrid Material for High Performance Supercapacitor Electrode and Photocatalyst, ACS Sustainable Chemistry and Engineering. 5 (2017) 4757–4770. https://doi.org/10.1021/acssuschemeng.7b00143.

[39] S. Aslam, T.H. Bokhari, T. Anwar, U. Khan, A. Nairan, K. Khan, Graphene oxide coated graphene foam based chemical sensor, Materials Letters. 235 (2019) 66–70. https://doi.org/10.1016/j.matlet.2018.09.164.

[40] D. Data, O. The, Diffraction Basics , Part 2 Overview Diffraction Basics , Part 2, Introduction to XRay Powder Diffraction. 2 (2009) 1–12.

[41] M. V Ananth, S. Pethkar, K. Dakshinamurthi, Distortion of MnO octahedra and electrochemical activity of 6 Nstutite-based MnO polymorphs for alkaline electrolytes-an FTIR 2 study, 1998.

[42] F. Barzegar, A. Bello, D. Momodu, M.J. Madito, J. Dangbegnon, N. Manyala, Preparation and characterization of porous carbon from expanded graphite for high energy density supercapacitor in aqueous electrolyte, Journal of Power Sources. 309 (2016) 245–253. https://doi.org/10.1016/j.jpowsour.2016.01.097.

[43] T. Gao, H. Fjellvåg, P. Norby, A comparison study on Raman scattering properties of α- and β-MnO2, Analytica Chimica Acta. 648 (2009) 235–239. https://doi.org/10.1016/j.aca.2009.06.059.

[44] H.U. Shah, F. Wang, M.S. Javed, R. Saleem, M.S. Nazir, J. Zhan, Z.U.H. Khan, M.U. Farooq, S. Ali, Synthesis, characterization and electrochemical properties of α-MnO2 nanowires as electrode material for supercapacitors, International Journal of Electrochemical Science. 13 (2018) 6426–6435. https://doi.org/10.20964/2018.07.48.

[45] V. Khomenko, E. Raymundo-Piñero, F. Béguin, Optimisation of an asymmetric manganese oxide/activated carbon capacitor working at 2 v in aqueous medium, Journal of Power Sources. 153 (2006) 183–190. https://doi.org/10.1016/j.jpowsour.2005.03.210.

[46] M. Huang, Y. Zhang, F. Li, L. Zhang, R.S. Ruoff, Z. Wen, Q. Liu, Self-assembly of mesoporous nanotubes assembled from interwoven ultrathin birnessite-type MnO2 nanosheets for asymmetric supercapacitors, Scientific Reports. 4 (2014). https://doi.org/10.1038/srep03878.